

# Frequency splitting of chiral phonons from broken time reversal symmetry in $\text{CrI}_3$

John Bonini,<sup>1</sup> Shang Ren,<sup>2</sup> David Vanderbilt,<sup>2</sup> Massimiliano Stengel,<sup>3,4</sup> Cyrus E. Dreyer,<sup>5,1</sup> and Sinisa Coh<sup>6</sup>

<sup>1</sup>*Center for Computational Quantum Physics, Flatiron Institute,  
162 5th Avenue, New York, New York 10010, USA*

<sup>2</sup>*Department of Physics and Astronomy, Rutgers University, Piscataway, New Jersey 08845-0849, USA*

<sup>3</sup>*Institut de Ciència de Materials de Barcelona (ICMAB-CSIC), Campus UAB, 08193 Bellaterra, Spain*

<sup>4</sup>*ICREA-Institució Catalana de Recerca i Estudis Avançats, 08010 Barcelona, Spain*

<sup>5</sup>*Department of Physics and Astronomy, Stony Brook University, Stony Brook, New York, 11794-3800, USA*

<sup>6</sup>*Materials Science and Mechanical Engineering, University of California Riverside, CA 92521, USA*

(Dated: September 1, 2022)

Conventional approaches for lattice dynamics based on static interatomic forces do not fully account for the effects of time-reversal-symmetry breaking in magnetic systems. Recent approaches to rectify this involve incorporating the first-order change in forces with atomic velocities under the assumption of adiabatic separation of electronic and nuclear degrees of freedom. In this work, we develop a first-principles method to calculate this velocity-force coupling in extended solids, and show via the example of ferromagnetic  $\text{CrI}_3$  that, due to the slow dynamics of the spins in the system, the assumption of adiabatic separation can result in large errors for splittings of zone-center chiral modes. We demonstrate that an accurate description of the lattice dynamics requires treating magnons and phonons on the same footing.

The atomic vibrations that are present in molecules and solids at zero and finite temperature play a crucial role in their thermodynamic and transport properties. First-principles calculations based on density-functional theory (DFT) have been established as a powerful tool for understanding and predicting lattice-dynamical properties, including phonon dispersion [1, 2] and electron-phonon coupling [3, 4]. The key quantity underlying the calculation of lattice dynamics is the interatomic force constant (IFC) matrix, which is constructed by finding derivatives of the nuclear forces with respect to nuclear positions, either directly via finite displacements or through density functional perturbation theory [1, 2].

In presence of magnetic ordering, the change in the electronic ground state compared to the nonmagnetic case propagates to the IFCs [5–9]. However, since it is defined and calculated as a static response function, the IFC matrix is invariant under time reversal by construction. Thus, a description of the nuclear dynamics based solely on the IFCs will not correctly reflect the vibration mode degeneracies in a magnetic system; instead, the phonon frequency spectrum will be determined by the *nonmagnetic* symmetry group.

There has been significant recent work on the explicit inclusion of time-reversal symmetry (TRS) breaking in the nuclear equations of motion via the *velocity* dependence of the interatomic forces, applied to models [10–13] and magnetic molecules [14]. This “velocity-force” coupling can be obtained from the nuclear Berry curvature, which describes the evolution of the phase of the electronic wavefunction with changes in nuclear coordinates [10, 11, 14]. A key result of including this coupling is that degenerate vibrational modes may split into non-degenerate chiral modes [15] with a well-defined finite angular momentum [14, 16], even at the Brillouin-zone center. Thus, the correct treatment of magnetic symmetry is crucial for elucidating the role of atomic vibrations

in thermal Hall [11, 17–20] and other effects involving TRS-broken lattice dynamics [21–28].

A key assumption underlying the velocity-force approach in previous works [10–14] is that the time scale for electronic dynamics is fast compared to nuclear dynamics. However, this may completely break down in some systems, e.g., when the nuclear Berry curvature results from nuclei coupling to *spins*, whose dynamics are not necessarily faster than the atomic vibrations. The breakdown of the adiabatic picture could have a profound effect on the predicted splitting of chiral phonon modes.

In this work, we illustrate such a situation using the bulk-layered magnetic insulator  $\text{CrI}_3$  as an example system. We first develop a DFT methodology amenable to both molecules and solids for computing phonons in the presence of velocity-force coupling. We apply this method to calculate the zone-center phonons in  $\text{CrI}_3$ , demonstrating the splitting of otherwise degenerate phonons into chiral modes. Next, we show that the velocity-force response is dominated by the canting of the spins on the Cr sites caused by atomic displacements. The dynamics of such spin canting are characterized by the zone-center magnon frequencies. The fact that magnon frequencies in  $\text{CrI}_3$  are on the same order or smaller than the optical phonon frequencies [29–36] means that we must treat spins and atomic displacements on the same footing. We develop a minimal model of this kind, and show that the adiabatic velocity-force approach can greatly overestimate the frequency splitting of the chiral modes.

We begin by reviewing the formalism of the velocity-force coupling from previous works [10–14], which we will refer to as the “Mead-Truhlar” (MT) approach. In order to simplify the discussion, we assume a finite system, generalizing to an infinite crystal below. The starting point of the derivation is the Born-Oppenheimer approximation, where the system wavefunction is factored into

nuclear and electronic parts such that the ground-state electronic wavefunction  $|\psi(\mathbf{R})\rangle$  depends parametrically on the nuclear coordinates  $\mathbf{R}$  [37]. Once the electronic degrees of freedom are integrated out, the effective Hamiltonian for the nuclear wavefunction becomes [13]

$$H_{\text{eff}} = \sum_{i\alpha} \frac{(p_{i\alpha} - \hbar A_{i\alpha}(\mathbf{R}))^2}{2m_i} + V_{\text{eff}}(\mathbf{R}), \quad (1)$$

where Roman indices (here  $i$ ) run over nuclei, Greek indices (here  $\alpha$ ) run over Cartesian directions,  $p_{i\alpha}$  is the momentum operator for nucleus  $i$  along direction  $\alpha$ , and  $m_i$  is the mass of nucleus  $i$ . Using the notation  $\partial_{i\alpha} = \partial/\partial R_{i\alpha}$ ,  $A_{i\alpha}(\mathbf{R}) = i \langle \psi(\mathbf{R}) | \partial_{i\alpha} \psi(\mathbf{R}) \rangle$  is a nuclear Berry potential, and  $V_{\text{eff}}(\mathbf{R}) = \epsilon(\mathbf{R}) + \sum_{i\alpha} \frac{\hbar^2}{2m_i} (\langle \partial_{i\alpha} \psi(\mathbf{R}) | \partial_{i\alpha} \psi(\mathbf{R}) \rangle - A_{i\alpha}(\mathbf{R})^2)$  is an effective scalar potential, where  $\epsilon(\mathbf{R})$  is the ground-state energy for a given fixed nuclear configuration. As first pointed out by Mead and Truhlar [13], the nuclear Berry potential  $A_{i\alpha}$  cannot always be made to vanish by changing the gauge of  $|\psi(\mathbf{R})\rangle$  via the choice of an  $\mathbf{R}$ -dependent phase factor.

The resulting vibrational modes are then found by solving the equations of motion which, to harmonic order in nuclear displacements, are given by [10–13]

$$\omega_n^2 \mathbf{M} \eta_n = (\mathbf{C} + i\omega_n \mathbf{G}) \eta_n. \quad (2)$$

Here  $\mathbf{M}$  is a diagonal nuclear mass matrix  $M_{i\alpha,j\beta} = m_i \delta_{i,j} \delta_{\alpha,\beta}$ ,  $\omega_n$  is the frequency of mode  $n$ , and  $\eta_n(\tau\alpha)$  is the component of the eigendisplacement of nucleus  $\tau$  along direction  $\alpha$  normalized so that  $\eta_n^\dagger \mathbf{M} \eta_m = \delta_{nm}$ .  $\mathbf{G}$  is the “velocity-force matrix,” whose elements  $G_{i\alpha,j\beta}$  relate the force on nucleus  $i$  along direction  $\alpha$  to the velocity of nucleus  $j$  along direction  $\beta$ , and is expressed as

$$G_{i\alpha,j\beta} = -2\hbar \text{Im} \langle \partial_{i\alpha} \psi(\mathbf{R}) | \partial_{j\beta} \psi(\mathbf{R}) \rangle, \quad (3)$$

which is just  $\hbar$  times the nuclear Berry curvature. The matrix  $\mathbf{C}$  is the IFC matrix, which we define to be  $C_{i\alpha,j\beta} = \partial_{i\alpha} \partial_{j\beta} \epsilon(\mathbf{R})$ . Note that following Eq. (1) one could alternatively define  $\mathbf{C}$  in terms of the Hessian of  $V_{\text{eff}}$ , which includes additional terms compared to the conventional IFC. However, the additional terms are higher order in the inverse nuclear mass and do not involve breaking of time-reversal symmetry, so that we neglect them in this work.

This formalism can be extended to the calculation of phonons in infinite crystals within DFT. We restrict ourselves to phonons at  $\Gamma$ , the Brillouin zone center, and work from a discrete set of DFT calculations on primitive-cell structures in which each sublattice displacement in turn is considered. The  $\mathbf{C}$  matrix is constructed in the usual way from finite differences of the forces, while  $\mathbf{G}$  is built from Berry phases computed over triangular configuration paths involving a given pair of sublattice-displaced structures and the undistorted structure. Berry phases are computed on a per-unit-cell basis for the Bloch manifold at each wave vector  $\mathbf{k}$  and then

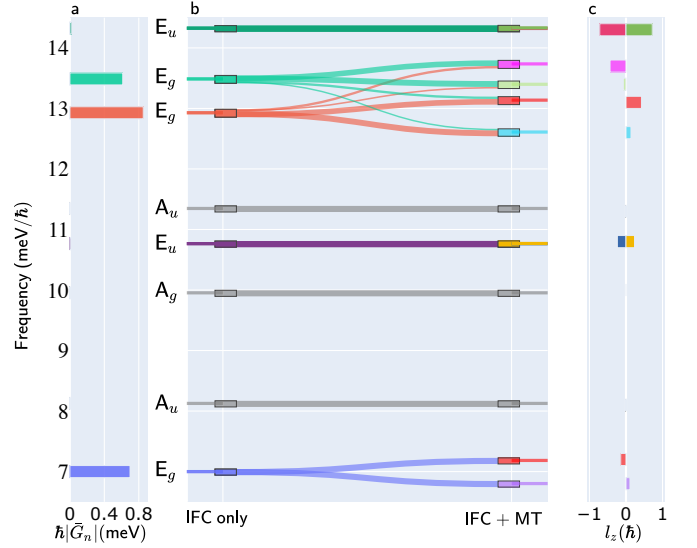


FIG. 1. For selected zone-center phonon modes of bulk ferromagnetic CrI<sub>3</sub>: (a) norm of the row of the velocity-force matrix  $\bar{\mathbf{G}}$  relevant to each phonon mode (b) phonon frequencies (labeled by irreducible representation) determined from just the interatomic force-constant matrix on the left of the panel (“IFC only”), and including the Mead-Truhlar correction on the right side (“IFC + MT”), illustrating the frequency splitting of degenerate modes; and (c) angular momentum values of each mode after the velocity force matrix contributions have been included. In (b) the thickness of the connection between modes corresponds to the magnitude of the overlap between their respective eigenvectors (connecting curves are arbitrary).

averaged over the Brillouin zone to get the desired  $\mathbf{G}$  matrix elements. The details are given in Sec. S1 of the supplemental material (SM) [38].

We perform calculations on CrI<sub>3</sub> in the ferromagnetic ground state using the VASP code [39–41], the local density approximation exchange-correlation functional [42], and projector-augmented wave potentials [43]. Semicore (3s, 3p) and (5s, 5p) states are included in the valence for Cr and I respectively. A  $5 \times 5 \times 5$  Monkhorst-Pack grid [44] is used to sample the Brillouin zone, and the energy cutoff for the plane-wave basis set is 520 eV. Spin-orbit coupling, which is essential to the physics described here, is included in all calculations.

As mentioned above, the conventional calculation of phonons neglects  $\mathbf{G}$  in Eq. (2), resulting in an equation of motion with TRS ( $\tilde{\omega}_n^2 \mathbf{M} \tilde{\eta}_n = \mathbf{C} \tilde{\eta}_n$ ). The resulting zone-center phonon modes with frequencies  $\tilde{\omega}_n$  can be represented with real eigendisplacements  $\tilde{\eta}_n$ . In CrI<sub>3</sub> the representation of these modes at the zone center can be decomposed into the real irreducible representations (irreps) of  $\bar{3}$  as  $4A_g \oplus 4A_u \oplus 4E_g \oplus 4E_u$ . The frequencies  $\tilde{\omega}_n$  range up to 32 meV (see the SM [38] Table SIII). We can consider the velocity-force coupling between phonon modes obtained from the IFC alone by defining  $\tilde{G}_{nm} = \tilde{\eta}_n^\dagger \mathbf{G} \tilde{\eta}_m$ ;  $\mathbf{G}$  is block diagonal, with each

block corresponding to a real irrep. Once  $\mathbf{G}$  is included in Eq. (2), TRS is broken and the twofold-degenerate  $E_u$  and  $E_g$  modes split, as the corresponding irreps further break up into complex one-dimensional representations.

In Fig. 1(b), we show a selection of zone-center phonon frequencies of bulk ferromagnetic  $\text{CrI}_3$  (see the SM [38] Table SIII for a complete list of frequencies). On the left side we plot  $\tilde{\omega}_n$ , i.e., the frequencies neglecting the velocity-force contribution, and on the right the frequencies including the velocity-force contribution via the MT approach (i.e.,  $\omega_n$ ). In Fig. 1(a) we plot the sum of the magnitudes of the velocity-force coupling terms relevant to each phonon eigenvector, as a measure of the strength of the coupling. We see that the  $E_g$  modes have the strongest coupling. We shall see why shortly.

The splitting of each of the two-fold degeneracies shown in Fig. 1(b) results in chiral phonons with well-defined angular momentum in the  $z$  direction (due to the symmetry of  $\text{CrI}_3$ ). For mode  $n$ , the angular momentum is found via  $l_z^{(n)} = 2\hbar \sum_{\tau} m_{\tau} \text{Im}[\eta_n^*(\tau x)\eta_n(\tau y)]$  [21, 45], where  $\tau$  runs over the atomic sublattices and  $m_{\tau}$  is the mass of nucleus  $\tau$ . If we neglect  $\mathbf{G}$  in Eq. (2), then the angular momentum of modes in a degenerate subspace spanned by  $(\tilde{\eta}_1, \tilde{\eta}_2)$  depend on the basis we choose. Clearly,  $l_z$  vanishes in the real basis  $\tilde{\eta}_n$  introduced above, while a complex “circularly polarized” combination of degenerate modes of the form  $\eta'_{\pm} = \tilde{\eta}_1 \pm i\tilde{\eta}_2$  will have equal and opposite  $l_z$  (since we are at the  $\Gamma$  point [16]), with the magnitude determined by the mode displacement patterns. Neglecting terms in the  $\bar{\mathbf{G}}$  matrix that mix different degenerate subspaces, the chiral modes after splitting will have exactly the eigendisplacements  $\eta'_{\pm}$ . Fig 1 (c) shows the angular momentum ( $l_z$ ) for each mode after the inclusion of the  $\mathbf{G}$  matrix. The fact that some of the split modes do not have equal and opposite  $l_z$  indicates mixing between the degenerate subspaces in  $\bar{\mathbf{G}}$ . See Sec. S4 of the SM for a full analysis of the angular momentum of the chiral modes[38].

We now analyze the mechanisms responsible for the velocity-force coupling in  $\text{CrI}_3$ . In this material, the magnetic moments reside on the Cr atoms and are initially oriented out of plane along  $z$ . We note that the modes with large  $\bar{\mathbf{G}}$  matrix elements in Fig. 1 are mostly those involving displacements of the I sublattices, which carry strong spin-orbit coupling. Under such displacements, it is natural that the Cr moments may cant, reflecting a local change in magnetic easy axis. This canting will result in a spin Berry curvature, and thus a contribution to  $\bar{\mathbf{G}}$ .

In fact, we find that for  $\text{CrI}_3$ , the spin Berry curvature is the dominant mechanism of velocity-force coupling. We demonstrate this by calculating the matrix elements of  $\bar{\mathbf{G}}$  under the assumption that only the spin-Berry-curvature mechanism is present. More specifically, we first approximate Eq. (3) as  $\bar{G}_{mn} \simeq B_{Ia,m} G_{Ia,Jb} B_{Jb,n}$ , where  $G_{Ia,Jb} = -2\hbar \text{Im}\langle \partial_{Ia}\psi | \partial_{Jb}\psi \rangle$  is the Berry curvature of the wavefunctions in the parameter space spanned by the Cr spins;  $B_{Ia,n} = \partial s_{Ia} / \partial \tilde{u}_n$  is a “spin canting matrix” describing the static change in the equilibrium spin

unit vector on magnetic Cr site  $I$  in direction  $a$  resulting from phonon perturbation  $n$ ; and  $\tilde{u}_n$  is the amplitude of mode  $n$  such that the set of atomic displacements are given by  $\tilde{u}_n \tilde{\eta}_n$  [46]. Under the assumption that the spin Berry curvature dominates, we can further approximate  $G_{Ia,Jb} = -S \delta_{IJ} \epsilon_{ab}$ , where spin  $S = 3\hbar/2$  for Cr and  $\epsilon_{ab}$  is the antisymmetric tensor; then

$$\bar{G}_{nm} = -S \sum_{Iab} \epsilon_{ab} B_{Ia,n} B_{Ib,m}. \quad (4)$$

A comparison between this spin-Berry approximation and the full Berry-phase calculation of the  $\bar{\mathbf{G}}$  matrix is presented in Table SII of the SM [38]. For some modes, the spin-Berry approximation accounts for only  $\sim 60\%$  of the full velocity-force contribution; this means that other contributions, e.g., “phonon-only Berry curvature” (the Berry curvature from atomic displacements at fixed spin) are significant. However, these modes exhibit relatively small splittings from the full velocity-force contribution, so the errors are not significant in absolute terms. For the two  $E_g$  modes that exhibit the largest splitting in the MT calculation [green, orange, and blue curves in Fig. 1(b)], the errors arising from this approximation are less than one percent.

This is a remarkable result, and is one of the main findings of the present work. By adopting the spin-Berry approximation, one can bypass the cumbersome computation of Berry phases for paths connecting distorted structures. Instead, all we need to take from the DFT calculations is the information about the spin canting in response to phonon distortions. In particular, it is now clear why the  $\bar{\mathbf{G}}$  tensor elements are so much smaller for the  $E_u$  modes; these are the ones that couple to the optical magnons, whose much larger stiffness strongly suppresses the spin canting.

A critical implication of the fact that the velocity-force coupling in  $\text{CrI}_3$  results from spin canting is that the assumption underlying the MT approach of Eqs. (1-3), namely, that all electronic dynamics are fast compared to that of the phonons, is clearly unfounded. This is because the relevant time scale for spin dynamics is that of the magnon frequencies in the system. The experimentally measured zone-center magnons of  $\text{CrI}_3$  have frequencies of 0.3 meV (i.e., the magnetocrystalline anisotropy) for the acoustic branch, and 17 meV for the optical branch [36], while the relevant phonons with the largest velocity-force coupling have frequencies in the range of 6-14 meV [see Fig. 1(b)].

Thus, an appropriate description of the low-energy dynamics must treat spins and phonons in this system on the same footing. To illustrate how this can be done, we focus on a single pair of  $E_g$  or  $E_u$  modes, which couple respectively either to an effective acoustic spin unit vector  $\mathbf{s} = (\mathbf{s}_1 + \mathbf{s}_2)/\sqrt{2}$  or its optical counterpart  $\mathbf{s} = (\mathbf{s}_1 - \mathbf{s}_2)/\sqrt{2}$ . Denoting the phonon mode amplitudes and momenta as  $(x, y)$  and  $(p_x, p_y)$ , the coupled

irrep	$\hbar\tilde{\omega}$ (meV)	splitting (meV)	
		MT	SP
$E_g$	6.9999	0.3820	0.0007
	12.9287	0.5270	0.0003
	13.4876	0.3368	0.0001
	29.8521	0.0244	$3 \times 10^{-6}$
$E_u$	10.7667	0.0043	0.0046
	14.3259	0.0090	0.0311
	27.8168	0.0349	0.0118

TABLE I. Frequency splitting of  $E_u$  and  $E_g$  zone-center phonon modes in  $\text{CrI}_3$ . Modes are labeled by their symmetry and frequency determined only from the interatomic force constants ( $\hbar\tilde{\omega}$ ). MT (“Mead-Truhlar”) refers to frequency splittings obtained by solving the equation of motion in Eq. (2), and SP (“spin-phonon”) corresponds to solving the coupled equations of motion in Eq. (6).

spin-phonon Hamiltonian takes the form

$$H = \frac{1}{2}(p_x^2 + p_y^2) + \frac{1}{2}\tilde{\omega}^2(x^2 + y^2) + \frac{1}{2}\alpha(s_x^2 + s_y^2) + \gamma(xs_x + ys_y). \quad (5)$$

Here  $\tilde{\omega}$  is the bare phonon frequency,  $\alpha = \partial^2 E / \partial s_x^2$  is the spin anisotropy energy, and  $\gamma = \partial^2 E / \partial x \partial s_x$  is the coupling between the spin and the pair of phonons (which have been chosen such that the  $xs_y$  and  $ys_x$  terms vanish). Note that the unperturbed magnon frequency is related to the anisotropy by  $\omega_m = \alpha/S$ , where  $S = 3\hbar/2$  is the Cr spin, and that the  $\mathbf{B}$  matrix introduced above reduces in this minimal model to  $B = \gamma/\alpha$ . Going over to circularly polarized coordinates via  $x_{\pm} = (x \pm iy)/\sqrt{2}$  and  $s_{\pm} = (s_x \pm is_y)/\sqrt{2}$ , the equations of motion become

$$\begin{aligned} (\tilde{\omega}^2 - \omega^2)x_{\pm} &= -\gamma s_{\pm}, \\ (\pm\omega_m - \omega)s_{\pm} &= \mp S^{-1}\gamma x_{\pm}, \end{aligned} \quad (6)$$

which are easily solved numerically.

In Table I, we compare the frequency splittings of doubly-degenerate modes determined by the adiabatic Mead-Truhlar (MT) approach and spin-phonon (SP) model. The last column in Table I presents the results for the spin-phonon model; the  $E_g$  modes couple to the acoustic magnon branch and the  $E_u$  modes to the optical branch (we use experimental [36] magnon frequencies of 0.3 and 17 meV, respectively) [47]. A more detailed comparison of Mead-Truhlar approach and spin-phonon model is presented in Sec. S2 of the SM[38].

In order to understand the general features of the spin-phonon mixing embodied in Eq. (6), we plot in Fig. 2 the solutions of Eq. (6) as a function of phonon frequency  $\tilde{\omega}$ , with the magnon frequency set to  $\omega_m = 17 \text{ meV}/\hbar$  (i.e., the optical branch [36]), and  $\gamma$  fixed at  $2 \text{ meV}^{3/2}/\hbar$ , a typical value for the  $E_u$  modes in  $\text{CrI}_3$  (since those are the phonons that couple to the optical magnon). The solid blue curve in the inset shows the splitting of the

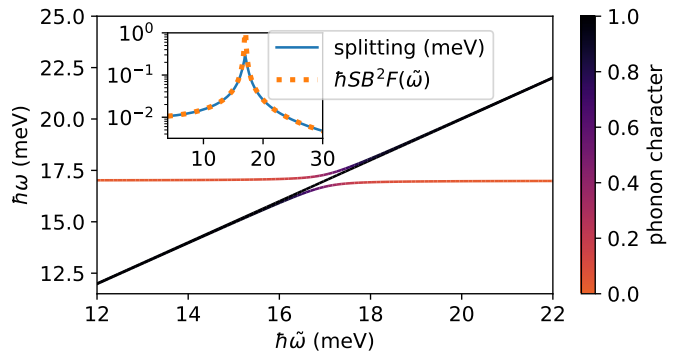


FIG. 2. Frequencies of interacting magnons and phonons as given by Eq. (6) as a function of uncoupled phonon frequency ( $\tilde{\omega}$ ) for  $\omega_m = 17 \text{ meV}/\hbar$  and  $\gamma = 2 \text{ meV}^{3/2}/\hbar$  which corresponds to a force velocity matrix element of  $\tilde{G} = 0.01 \text{ meV}/\hbar$ . The color of the curve indicates the magnitude of the phonon component of the mode eigenvector. The inset shows the splitting of the modes as well as the heuristic for splitting away from resonance,  $\hbar SB^2 F(\tilde{\omega})$ , where  $F = |1 - (\tilde{\omega}/\omega_m)^2|^{-1}$ .

modes with dominant phonon character also as a function of  $\tilde{\omega}$ . Outside of the small “resonant” regime  $\tilde{\omega} \simeq \omega_m$ , where significant magnon-phonon hybridization occurs, the mode splitting is well described by  $SB^2F$  (see orange dashed curve in inset of Fig. 2), where  $SB^2$  is the relevant force-velocity term in the adiabatic spin-Berry approximation [i.e., Eq. (4)] and  $F = |1 - (\tilde{\omega}/\omega_m)^2|^{-1}$ . At small  $\tilde{\omega}$ , the magnon can be treated as a high-energy degree of freedom which renormalizes the phonons, and the splitting from the MT approach is recovered. Increasing  $\tilde{\omega}$  toward  $\omega_m$  enhances the splitting of modes over the value at the adiabatic (MT) limit, peaking at the point where the magnon and phonon frequencies coincide and the modes have maximum hybridization. Above  $\omega_m$ , the splitting decreases from its peak value, but is still enhanced over that determined by the MT approach for a range of  $\tilde{\omega}$ . At  $\tilde{\omega} \gg \omega_m$  the splitting is suppressed, and vanishes as  $\tilde{\omega} \rightarrow \infty$ .

This behavior is reflected in the splittings given in Table I. Two of the three  $E_u$  modes which couple to the optical magnon have frequencies below  $\omega_m = 17 \text{ meV}/\hbar$ , but still in ranges where the splitting is enhanced above the adiabatic MT limit. The physical interpretation here is that the phonons are becoming hybridized with the magnon instead of just having their frequencies renormalized by it. However, since the splittings in the adiabatic limit (and thus the corresponding  $\mathbf{G}$  matrix elements) are proportional to  $\omega_m^{-2}$ , the splittings remain quite small. The largest frequency  $E_u$  mode has  $\omega_m \ll \tilde{\omega}$ , so that the splitting is reduced compared to values obtained from the velocity-force approach.

The  $E_g$  modes couple to the acoustic magnon ( $\omega_m = 0.3 \text{ meV}/\hbar$ ), so for all  $E_g$  modes  $\tilde{\omega} \gg \omega_m$ , which is precisely the opposite of the limit in which the adiabatic velocity-force theory is applicable. This results in the drastic reduction ( $F \ll 1$ ) in the splitting of the  $E_g$

modes in Table I compared to the MT description in Eq. (2). The physical interpretation of this regime is that the Cr spins cannot keep up with the phonons, and thus the area swept out from the spin canting is greatly reduced compared to the assumption that they follow the nuclear motion adiabatically.

Clearly, these results have significant implications for experimental measurements of chiral phonons in CrI<sub>3</sub>. Optical techniques, possibly utilizing circular polarization, constitute a powerful tool for studying such properties [22, 25, 48–50]. The strongly suppressed frequency splitting (SP column of Table I) of the Raman-active  $E_g$  modes is likely to be difficult to detect. This is consistent with recent work on CrBr<sub>3</sub>, a related system, which found signatures of the chiral phonons but did not report a splitting of these modes [25]. The larger, though still quite modest, splitting of the  $E_u$  modes could in principle be measured by peak shifts in infrared absorption [51], while direct detection of chirality would require circularly polarized infrared spectroscopy as in Refs. [48, 49].

More generally, our results also have several implications for finding other systems with a large splitting of chiral phonon modes at  $\Gamma$ . In materials like CrI<sub>3</sub>, where the spin-Berry mechanism is responsible for the majority of the velocity-force coupling, it is most promising to look for (or engineer via, e.g., strain or magnetic field) cases where the relevant phonon and magnon frequencies coincide. This avoids the suppression of the splitting in the  $\tilde{\omega} \gg \omega_m$  regime, and the small spin canting likely when  $\omega_m \gg \tilde{\omega}$ . Systems with lower-frequency optical magnons that maintain similar or larger spin-phonon coupling  $\gamma$

are also strong candidates for observing larger effects. In any case, we can see from Table I that correctly accounting for the relative dynamics of spins versus phonons is necessary to avoid significantly overestimating the splitting of certain chiral modes.

In conclusion, we have developed and implemented a first-principles methodology for capturing time-reversal-symmetry-broken lattice dynamics in magnetic solids, and applied it to the case of bulk ferromagnetic CrI<sub>3</sub>. We show that in this system, the previously-made assumption of fast electron dynamics compared to the lattice breaks down, since the relevant coupling is between Cr spins and atomic displacements. With a minimal model, we demonstrate that spins and phonons must be treated on the same footing to avoid large qualitative errors in the splitting of chiral modes.

## ACKNOWLEDGMENTS

CED, DV, and SC acknowledge support from the National Science Foundation under Grants DMR-1918455, DMR-1954856, and DMR-1848074 respectively. The Flatiron Institute is a division of the Simons Foundation. M.S. acknowledges the support of Ministerio de Ciencia y Innovación (MICINN-Spain) through Grants No. PID2019-108573GB-C22 and CEX2019-000917-S; of Generalitat de Catalunya (Grant No. 2017 SGR1506); and of the European Research Council (ERC) through Grant No. 724529.

- 
- [1] X. Gonze and C. Lee, Dynamical matrices, Born effective charges, dielectric permittivity tensors, and interatomic force constants from density-functional perturbation theory, *Phys. Rev. B* **55**, 10355 (1997).
  - [2] S. Baroni, S. de Gironcoli, A. Dal Corso, and P. Giannozzi, Phonons and related crystal properties from density-functional perturbation theory, *Reviews of Modern Physics* **73**, 515–562 (2001).
  - [3] F. Giustino, Electron-phonon interactions from first principles, *Rev. Mod. Phys.* **89**, 015003 (2017).
  - [4] B. Monserrat, Electron-phonon coupling from finite differences, *Journal of Physics: Condensed Matter* **30**, 083001 (2018).
  - [5] M. Posternak, A. Baldereschi, S. Massidda, and N. Marzari, Maximally localized Wannier functions in antiferromagnetic MnO within the FLAPW formalism, *Physical Review B* **65**, 184422 (2002).
  - [6] J. H. Lee and K. M. Rabe, Large spin-phonon coupling and magnetically induced phonon anisotropy in SrMO<sub>3</sub> perovskites ( $M = \text{V, Cr, Mn, Fe, Co}$ ), *Phys. Rev. B* **84**, 104440 (2011).
  - [7] J. Hong, A. Stroppa, J. Íñiguez, S. Picozzi, and D. Vanderbilt, Spin-phonon coupling effects in transition-metal perovskites: A DFT +  $U$  and hybrid-functional study, *Phys. Rev. B* **85**, 054417 (2012).
  - [8] K. Wang, W. Zhou, Y. Cheng, M. Zhang, H. Wang, and G. Zhang, Magnetic order-dependent phonon properties in 2D magnet CrI<sub>3</sub>, *Nanoscale* **13**, 10882 (2021).
  - [9] J. Wu, Y. Yao, M.-L. Lin, M. Rösner, Z. Du, K. Watanabe, T. Taniguchi, P.-H. Tan, S. Haas, and H. Wang, Spin-phonon coupling in ferromagnetic monolayer chromium tribromide, *Advanced Materials* **34**, 2108506 (2022).
  - [10] T. Qin, J. Zhou, and J. Shi, Berry curvature and the phonon Hall effect, *Physical Review B* **86**, 104305 (2012).
  - [11] T. Saito, K. Misaki, H. Ishizuka, and N. Nagaosa, Berry phase of phonons and thermal Hall effect in nonmagnetic insulators, *Phys. Rev. Lett.* **123**, 255901 (2019).
  - [12] D. Saporov, B. Xiong, Y. Ren, and Q. Niu, Lattice dynamics with molecular Berry curvature: Chiral optical phonons, *Phys. Rev. B* **105**, 064303 (2022).
  - [13] C. A. Mead and D. G. Truhlar, On the determination of Born-Oppenheimer nuclear motion wave functions including complications due to conical intersections and identical nuclei, *The Journal of Chemical Physics* **70**, 2284 (1979).
  - [14] O. Bistoni, F. Mauri, and M. Calandra, Intrinsic vibrational angular momentum from nonadiabatic effects in noncollinear magnetic molecules, *Phys. Rev. Lett.* **126**, 225703 (2021).

- [15] L. Zhang and Q. Niu, Chiral phonons at high-symmetry points in monolayer hexagonal lattices, *Phys. Rev. Lett.* **115**, 115502 (2015).
- [16] S. Coh, Classification of materials with phonon angular momentum and microscopic origin of angular momentum (2019), [arXiv:1911.05064 \[cond-mat.mtrl-sci\]](https://arxiv.org/abs/1911.05064).
- [17] G. Grissonnanche, A. Legros, S. Badoux, E. Lefrançois, V. Zlatko, M. Lizaire, F. Laliberté, A. Gourgout, J. S. Zhou, S. Pyon, T. Takayama, H. Takagi, S. Ono, N. Doiron-Leyraud, and L. Taillefer, Giant thermal Hall conductivity in the pseudogap phase of cuprate superconductors, *Nature* **571**, 376 (2019).
- [18] J.-Y. Chen, S. A. Kivelson, and X.-Q. Sun, Enhanced thermal Hall effect in nearly ferroelectric insulators, *Phys. Rev. Lett.* **124**, 167601 (2020).
- [19] X. Li, B. Fauqué, Z. Zhu, and K. Behnia, Phonon thermal Hall effect in strontium titanate, *Phys. Rev. Lett.* **124**, 105901 (2020).
- [20] H. Zhang, C. Xu, C. Carnahan, M. Sretenovic, N. Suri, D. Xiao, and X. Ke, Anomalous thermal Hall effect in an insulating van der Waals magnet, *Phys. Rev. Lett.* **127**, 247202 (2021).
- [21] L. Zhang and Q. Niu, Angular momentum of phonons and the Einstein-de Haas effect, *Phys. Rev. Lett.* **112**, 085503 (2014).
- [22] H. Zhu, J. Yi, M.-Y. Li, J. Xiao, L. Zhang, C.-W. Yang, R. A. Kaindl, L.-J. Li, Y. Wang, and X. Zhang, Observation of chiral phonons, *Science* **359**, 579 (2018).
- [23] H. Chen, W. Zhang, Q. Niu, and L. Zhang, Chiral phonons in two-dimensional materials, *2D Materials* **6**, 012002 (2018).
- [24] J. H. Mentink, M. I. Katsnelson, and M. Leshchko, Quantum many-body dynamics of the Einstein-de Haas effect, *Phys. Rev. B* **99**, 064428 (2019).
- [25] T. Yin, K. A. Ulman, S. Liu, A. Granados del Águila, Y. Huang, L. Zhang, M. Serra, D. Sedmidubsky, Z. Sofer, S. Y. Quek, and Q. Xiong, Chiral phonons and giant magneto-optical effect in CrBr<sub>3</sub> 2D magnet, *Advanced Materials* **33**, 2101618 (2021).
- [26] H. Chen, W. Wu, J. Zhu, Z. Yang, W. Gong, W. Gao, S. A. Yang, and L. Zhang, Chiral phonon diode effect in chiral crystals, *Nano Letters* **22**, 1688 (2022), pMID: 35148114.
- [27] A. Baydin, F. G. G. Hernandez, M. Rodriguez-Vega, A. K. Okazaki, F. Tay, G. T. Noe, I. Katayama, J. Takeda, H. Nojiri, P. H. O. Rappl, E. Abramof, G. A. Fiete, and J. Kono, Magnetic control of soft chiral phonons in PbTe, *Phys. Rev. Lett.* **128**, 075901 (2022).
- [28] D. M. Juraschek, T. Neuman, and P. Narang, Giant effective magnetic fields from optically driven chiral phonons in 4f paramagnets, *Phys. Rev. Research* **4**, 013129 (2022).
- [29] W.-B. Zhang, Q. Qu, P. Zhu, and C.-H. Lam, Robust intrinsic ferromagnetism and half semiconductivity in stable two-dimensional single-layer chromium trihalides, *J. Mater. Chem. C* **3**, 12457 (2015).
- [30] J. L. Lado and J. Fernández-Rossier, On the origin of magnetic anisotropy in two dimensional CrI<sub>3</sub>, *2D Materials* **4**, 035002 (2017).
- [31] L. Webster and J.-A. Yan, Strain-tunable magnetic anisotropy in monolayer CrCl<sub>3</sub>, CrBr<sub>3</sub>, and CrI<sub>3</sub>, *Phys. Rev. B* **98**, 144411 (2018).
- [32] N. Richter, D. Weber, F. Martin, N. Singh, U. Schwingenschlögl, B. V. Lotsch, and M. Kläui, Temperature-dependent magnetic anisotropy in the layered magnetic semiconductors CrI<sub>3</sub> and CrBr<sub>3</sub>, *Phys. Rev. Materials* **2**, 024004 (2018).
- [33] I. Lee, F. G. Utermohlen, D. Weber, K. Hwang, C. Zhang, J. van Tol, J. E. Goldberger, N. Trivedi, and P. C. Hammel, Fundamental spin interactions underlying the magnetic anisotropy in the Kitaev ferromagnet CrI<sub>3</sub>, *Phys. Rev. Lett.* **124**, 017201 (2020).
- [34] C. Bacaksiz, D. Šabani, R. M. Menezes, and M. V. Milošević, Distinctive magnetic properties of CrI<sub>3</sub> and CrBr<sub>3</sub> monolayers caused by spin-orbit coupling, *Phys. Rev. B* **103**, 125418 (2021).
- [35] L. Ke and M. I. Katsnelson, Electron correlation effects on exchange interactions and spin excitations in 2D van der Waals materials, *npj Computational Materials* **7**, 4 (2021), [arXiv:2007.14518](https://arxiv.org/abs/2007.14518).
- [36] J. Cenker, B. Huang, N. Suri, P. Thijssen, A. Miller, T. Song, T. Taniguchi, K. Watanabe, M. A. McGuire, D. Xiao, and X. Xu, Direct observation of two-dimensional magnons in atomically thin CrI<sub>3</sub>, *Nature Physics* **17**, 20 (2021).
- [37] M. Born and K. Huang, *Dynamical Theory of Crystal Lattices*, International Series of Monographs on Physics (Oxford University Press, Walton Street, Oxford OX2 6DP, UK, 1954).
- [38] See supplemental material [URL to be inserted by publisher] for...
- [39] G. Kresse and J. Hafner, Ab initio molecular dynamics for liquid metals, *Phys. Rev. B* **47**, 558 (1993).
- [40] G. Kresse and J. Furthmüller, Efficient iterative schemes for ab initio total-energy calculations using a plane-wave basis set, *Phys. Rev. B* **54**, 11169 (1996).
- [41] G. Kresse and D. Joubert, From ultrasoft pseudopotentials to the projector augmented-wave method, *Phys. Rev. B* **59**, 1758 (1999).
- [42] J. P. Perdew and A. Zunger, Self-interaction correction to density-functional approximations for many-electron systems, *Phys. Rev. B* **23**, 5048 (1981).
- [43] P. E. Blöchl, Projector augmented-wave method, *Phys. Rev. B* **50**, 17953 (1994).
- [44] H. J. Monkhorst and J. D. Pack, Special points for Brillouin-zone integrations, *Phys. Rev. B* **13**, 5188 (1976).
- [45] A. G. McLellan, Angular momentum states for phonons and a rotationally invariant development of lattice dynamics, *Journal of Physics C: Solid State Physics* **21**, 1177 (1988).
- [46] Here  $a$  runs only over  $x, y$  directions corresponding to the two possible tilt angles. We have assumed the total magnitude of the spin is unchanged and that tilt angles are small so that  $S_{Ix} = S \sin(\theta_{Ix}) \approx SS_{Ix}$ .
- [47] A more general description of spin-phonon coupling, treating all relevant nuclear and spin degrees of freedom simultaneously, will be presented in a forthcoming communication.
- [48] L. A. Nafie, T. A. Keiderling, and P. J. Stephens, Vibrational circular dichroism, *Journal of the American Chemical Society* **98**, 2715 (1976).
- [49] R. Laiho, On the optical absorption and the magnetic circular dichroism of the transparent ferromagnet K<sub>2</sub>CuF<sub>4</sub>, *physica status solidi (b)* **69**, 579 (1975).

- [50] L. Du, J. Tang, Y. Zhao, X. Li, R. Yang, X. Hu, X. Bai, X. Wang, K. Watanabe, T. Taniguchi, D. Shi, G. Yu, X. Bai, T. Hasan, G. Zhang, and Z. Sun, Lattice dynamics, phonon chirality, and spin-phonon coupling in 2d itinerant ferromagnet  $\text{Fe}_3\text{GeTe}_2$ , [Advanced Functional Materials](#) **29**, 1904734 (2019).
- [51] L. Tomarchio, S. Macis, L. Mosesso, L. T. Nguyen, A. Grilli, M. C. Guidi, R. J. Cava, and S. Lupi, Low energy electrodynamics of  $\text{CrI}_3$  layered ferromagnet, [Scientific Reports](#) **11**, 23405 (2021).

# Supplemental Material: Frequency splitting of chiral phonons from broken time reversal symmetry in CrI<sub>3</sub>

John Bonini,<sup>1</sup> Shang Ren,<sup>2</sup> David Vanderbilt,<sup>2</sup> Massimiliano Stengel,<sup>3,4</sup> Cyrus E. Dreyer,<sup>5,1</sup> and Sinisa Coh<sup>6</sup>

<sup>1</sup>*Center for Computational Quantum Physics, Flatiron Institute,  
162 5th Avenue, New York, New York 10010, USA*

<sup>2</sup>*Department of Physics and Astronomy, Rutgers University, Piscataway, New Jersey 08845-0849, USA*

<sup>3</sup>*Institut de Ciència de Materials de Barcelona (ICMAB-CSIC), Campus UAB, 08193 Bellaterra, Spain*

<sup>4</sup>*ICREA-Institució Catalana de Recerca i Estudis Avançats, 08010 Barcelona, Spain*

<sup>5</sup>*Department of Physics and Astronomy, Stony Brook University, Stony Brook, New York, 11794-3800, USA*

<sup>6</sup>*Materials Science and Mechanical Engineering, University of California Riverside, CA 92521, USA*

(Dated: September 1, 2022)

## S1. FINITE DIFFERENCE APPROACH FOR CALCULATING BERRY CURVATURES

Here we provide some details of our density-functional theory (DFT) finite-displacement approach for calculating the interatomic force constant (IFC) matrix  $\mathbf{C}$ , and the adiabatic velocity-force coupling  $\mathbf{G}$ . The IFC matrix is calculated in the conventional way [S1, S2] by displacing each nucleus  $i$  by distance  $\delta\tau = 0.015 \text{ \AA}$  in each Cartesian direction, and calculating the resulting forces. The wave functions from these displaced calculations are saved for the following steps. The full velocity-force matrix elements [see Eq. 3 in the main text] are calculated by considering closed paths among these displaced configurations, as discussed in Sec. S1 A, while the matrix elements  $\mathbf{G}$  under the spin-Berry approximation [see main text Eq. 4] are determined by calculating the canting of the Cr spins from the same displacements, see Sec. S1 B.

### A. Velocity-force coupling

Stokes' theorem equates the integral of the Berry curvature over some region in parameter space with the integral of the Berry potential along the boundary of that region. We consider the Berry phase  $\phi_{i\alpha,j\beta}$  corresponding to a state evolving adiabatically along a triangular path from the ground state structure to displacement  $\tau_{i\alpha}$ , then to displacement  $\tau_{j\beta}$ , and back to the ground state. Assuming  $\delta\tau$  is small enough that the Berry curvature is constant over the area of the path,

$$G_{i\alpha,j\beta} = \frac{2\hbar\phi_{i\alpha,j\beta}}{|\tau_{i\alpha} \wedge \tau_{j\beta}|}, \quad (\text{S1})$$

where  $\tau_{i\alpha}$  is a displacement of nucleus  $i$  in direction  $\alpha$ . Since these displacements are chosen as orthogonal, the wedge product is simply  $\delta\tau^2$ . For a finite system, letting  $\psi(\tau_{i\alpha})$  be the ground state electronic wave function for the displaced structure, we compute the three-point discrete Berry phase

$$\phi_{i\alpha,j\beta} = -\text{Im} \ln [\langle \psi(0) | \psi(\tau_{i\alpha}) \rangle \langle \psi(\tau_{i\alpha}) | \psi(\tau_{j\beta}) \rangle \langle \psi(\tau_{j\beta}) | \psi(0) \rangle], \quad (\text{S2})$$

where  $\psi(0)$  indicates the ground state without displacements. For a solid calculated within DFT, Eq. (S2) holds for the single-band case, except that we define  $\psi_{\mathbf{k}}(\tau_{i\alpha})$  to be the Kohn-Sham Bloch wavefunctions for the displaced structures, and we must average over  $k$  points in the first Brillouin zone. That is,

$$\phi_{i\alpha,j\beta} = -\frac{1}{N_{\mathbf{k}}} \sum_{\mathbf{k}} \text{Im} \ln [\langle \psi_{\mathbf{k}}(0) | \psi_{\mathbf{k}}(\tau_{i\alpha}) \rangle \langle \psi_{\mathbf{k}}(\tau_{i\alpha}) | \psi_{\mathbf{k}}(\tau_{j\beta}) \rangle \langle \psi_{\mathbf{k}}(\tau_{j\beta}) | \psi_{\mathbf{k}}(0) \rangle], \quad (\text{S3})$$

where  $\mathbf{k}$  is the Bloch wave vector and  $N_{\mathbf{k}}$  is number of  $k$  points in the Brillouin zone. The generalization of the discrete Berry phase for multiple bands can be found in Ref. S3, and is given by

$$\phi_{i\alpha,j\beta} = -\frac{1}{N_{\mathbf{k}}} \sum_{\mathbf{k}} \text{Im} \ln \text{Det}[M^k(0, \tau_{i\alpha})M^k(\tau_{i\alpha}, \tau_{j\beta})M^k(\tau_{j\beta}, 0)], \quad (\text{S4})$$

where the overlap matrices are defined as

$$M_{mn}^k(\tau, \tau') = \langle \psi_{m\mathbf{k}}(\tau) | \psi_{n\mathbf{k}}(\tau') \rangle \quad (\text{S5})$$

with  $m$  and  $n$  being the band indices.



## B. Velocity-force coupling under spin-Berry approximation

Within the spin-Berry approximation of Eq. 4, the matrix elements of  $\mathbf{G}$  are obtained from the response of the localized spins to atomic displacements. The assumption is that for a given closed path along which nuclear coordinates are changed, the Berry phase is given by the sum of the Berry phases picked up by each local spin along that path. Each spin picks up a phase equal minus to the total spin magnitude,  $-S$  (in our case  $S = 3/2$ ), times the solid angle on the Bloch sphere that is swept out along the path. For small canting angles and with all spins pointing along  $z$  in the ground state,  $\mathbf{G}$  is then constructed using Eq. S1 with  $\phi_{i\alpha,j\beta}$  now given by

$$\phi_{i\alpha,j\beta} = -\frac{S}{2} \sum_I (s_{Ix}(\tau_{i\alpha})s_{Iy}(\tau_{j\beta}) - s_{Iy}(\tau_{i\alpha})s_{Ix}(\tau_{j\beta})). \quad (\text{S6})$$

Equivalently,  $\mathbf{G}$  could be constructed from the derivatives of the spins with respect to atomic displacements as in Eq. 4

Irrep	$\hbar\tilde{\omega}$ (meV)	$s_{1x}$	$s_{1y}$	$s_{2x}$	$s_{2y}$
$E_g$	6.9999	-0.01047	0.00416	-0.01047	0.00416
		-0.00416	-0.01047	-0.00416	-0.01047
	12.9287	-0.00253	-0.01356	-0.00253	-0.01356
		-0.01356	0.00253	-0.01356	0.00253
	13.4876	0.00521	-0.00847	0.00521	-0.00847
		-0.00847	-0.00521	-0.00847	-0.00521
29.8521	0.00028	-0.00317	0.00028	-0.00317	
	0.00317	0.00028	0.00317	0.00028	
$E_u$	10.7667	0.00008	-0.00095	-0.00008	0.00095
		0.00095	0.00008	-0.00095	-0.00008
	14.3259	0.00101	0.00142	-0.00101	-0.00142
		0.00142	-0.00101	-0.00142	0.00101
	27.8168	0.00251	-0.00057	-0.00251	0.00057
		-0.00057	-0.00251	0.00057	0.00251

TABLE SI. Derivative of spin canting of Cr atoms 1 and 2 in Cartesian directions  $x$  and  $y$  with respect to amplitudes of  $E_g$  and  $E_u$  modes in ferromagnetic  $\text{CrI}_3$ . The units for the spin derivatives with respect to mode amplitude are  $\sqrt{\text{meV}/\hbar}$ . Degenerate mode pairs are labeled by their unperturbed frequencies  $\hbar\tilde{\omega}$ ; the two rows for each entry correspond to the two modes comprising the pair in a real basis.

## S2. CONTRIBUTION OF SPIN CANTING TO ADIABATIC VELOCITY-FORCE COUPLING

In Table SII we compare the velocity-force coupling computed under the Mead-Truhlar (MT) approach (i.e., assuming adiabatic electron dynamics), using the  $\mathbf{G}$  matrix obtained from the the full wave function Berry curvature as in Eq. 3 of the main text (labeled “W”), with the  $\mathbf{G}$  matrix obtained from the spin-Berry approximation of Eq. 4 of the main text (labeled “S”). Modes are labeled by their irrep and frequency as determined only from the IFC matrix ( $\tilde{\omega}$ ). For each pair we show the magnitude of the matrix element between the degenerate modes ( $G_{ij}$ ) and frequency splitting  $\Delta\omega$ . Deviations between matrix elements and frequency splitting occur only when  $\mathbf{G}$  induces mixing between the degenerate subspaces. We see that indeed, the spin-Berry contribution accounts for the majority of spin-phonon coupling. For the three lowest-frequency  $E_g$  modes and the  $E_u$  mode near 14 meV, the agreement is excellent, within 1%. For the highest-frequency  $E_g$  mode and the other two  $E_u$  modes, the spin-Berry contribution has a discrepancy of 25-43%. This indicates that other terms, such as the “phonon-only Berry curvature” resulting from atomic displacements at fixed spins, may have a significant contribution. In any case, within the MT theory, the splittings of the highest-frequency  $E_g$  mode and all of the  $E_u$  modes are quite small, so the error in absolute terms is not large.

## S3. FREQUENCIES OF ALL MODES

In the spin-phonon model (SP) of Eq. 5 the  $\gamma$  parameter is related to the magnitude of the  $\bar{\mathbf{G}}$  matrix elements coupling degenerate modes  $i$  and  $j$  by  $\gamma = \omega_m \sqrt{S\bar{G}_{ij}}$ . Here the natural choice for the  $\bar{G}_{ij}$  value from which to obtain

Irrep	$\hbar\tilde{\omega}$ (meV)	MT (W)		MT (S)	
		$\hbar\tilde{G}_{ij}$ (meV)	$\hbar\Delta\omega$ (meV)	$\hbar\tilde{G}_{ij}$ (meV)	$\hbar\Delta\omega$ (meV)
$E_g$	6.9999	0.3825	0.3820	0.3808	0.3803
	12.9287	0.5685	0.5270	0.5712	0.5293
	13.4876	0.2948	0.3368	0.2968	0.3391
	29.8521	0.0243	0.0244	0.0305	0.0306
$E_u$	10.7667	0.0043	0.0043	0.0027	0.0027
	14.3259	0.0090	0.0090	0.0091	0.0091
	27.8168	0.0349	0.0349	0.0199	0.0199

TABLE II. Comparison of velocity-force matrix elements ( $\tilde{G}_{ij} = \eta_i^\dagger \mathbf{G} \eta_j$ ) and frequency splitting ( $\Delta\omega$ ) of  $E_u$  and  $E_g$  zone center phonon modes in  $\text{CrI}_3$  computed with Berry curvatures obtained from wavefunction overlaps (W) and with Berry curvatures obtained by the solid angle swept out by magnetic moments on the Cr sites (S). Modes are labelled by their irrep and frequency determined only from the interatomic force constants ( $\hbar\tilde{\omega}$ ).

$\gamma$  is that of the spin-Berry approximation, as  $\gamma$  is really defined in terms of spin-phonon coupling. It is in general possible for a system to have a nonzero MT term even when evaluated at fixed spin, as well as a distinct  $\gamma$  coupling to spin degrees of freedom; this will be explored in subsequent work. While the SP values presented here incorporate nonadiabatic effects not present in the nuclear MT theory, they do not include any coupling of modes outside the degenerate subspace (that is, there is no mixing between modes with distinct  $\tilde{\omega}$ ).

In order to present the effects of these different levels of approximation independently, we consider four possible  $\mathbf{G}$  matrices for MT (labeled W, w, S, and s) and two possible  $\mathbf{G}$  matrices for SP (w and s). As above, W and S correspond to  $\mathbf{G}$  matrices obtained using Eq. 3 and Eq. 4 of the main text, respectively. Results labeled “w” and “s” correspond to setting all couplings between nondegenerate  $\tilde{\omega}$  equal to zero in “W” and “S”  $\mathbf{G}$  matrices respectively. In Table SIII we give the frequencies of all of the optical modes (including the singly-degenerate ones), from the IFC matrix only ( $\hbar\tilde{\omega}$ ), with adiabatic Mead-Truhlar (MT), and in the spin-phonon model (SP), for each of these cases.

$\hbar\tilde{\omega}$	MT (W)	MT (w)	SP (w)	MT (S)	MT (s)	SP (s)
6.9999	6.8021	6.8113	6.9996	6.8030	6.8122	6.9996
6.9999	7.1841	7.1938	7.0003	7.1832	7.1929	7.0003
8.1265	8.1265	8.1265	8.1265	8.1265	8.1265	8.1265
9.9535	9.9535	9.9535	9.9535	9.9535	9.9535	9.9535
10.7667	10.7645	10.7645	10.7575	10.7653	10.7653	10.7608
10.7667	10.7688	10.7688	10.7646	10.7680	10.7680	10.7653
11.3471	11.3471	11.3471	11.3471	11.3471	11.3471	11.3471
12.9287	12.6100	12.6475	12.9285	12.6082	12.6462	12.9285
12.9287	13.1369	13.2161	12.9288	13.1375	13.2174	12.9288
13.4876	13.3989	13.3410	13.4875	13.3983	13.3400	13.4875
13.4876	13.7357	13.6358	13.4877	13.7374	13.6368	13.4877
14.3259	14.3214	14.3214	14.2924	14.3213	14.3213	14.2919
14.3259	14.3304	14.3304	14.3230	14.3305	14.3305	14.3230
16.5013	16.5013	16.5013	16.5013	16.5013	16.5013	16.5013
16.6023	16.6023	16.6023	16.6023	16.6023	16.6023	16.6023
26.5081	26.5081	26.5081	26.5081	26.5081	26.5081	26.5081
27.8168	27.7993	27.7993	27.8127	27.8068	27.8068	27.8145
27.8168	27.8342	27.8342	27.8335	27.8267	27.8267	27.8263
29.8521	29.8407	29.8400	29.8521	29.8376	29.8369	29.8521
29.8521	29.8650	29.8643	29.8521	29.8681	29.8674	29.8521
31.7361	31.7361	31.7361	31.7361	31.7361	31.7361	31.7361

TABLE SIII. Frequencies in meV of optical phonon modes of ferromagnetic  $\text{CrI}_3$  at the zone-center computed with different levels of theory.  $\hbar\tilde{\omega}$  labels frequencies computed using only the force constant matrix. MT refers to frequencies computed within the adiabatic velocity-force, or Mead-Truhlar formalism. SP refers to frequencies computed in the spin-phonon model. Labels W, w, S, and s refer to different couplings used in each calculation as explained in Sec. S3.

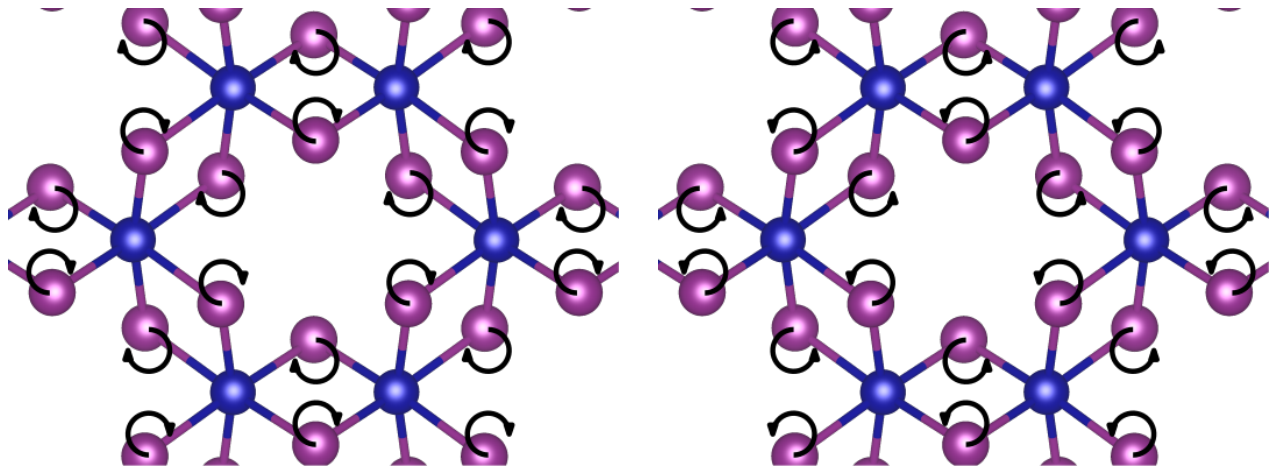


FIG. S1. Schematic of chiral trajectories of selected zone-center phonon modes in a single layer of bulk CrI<sub>3</sub>. In the presence of time-reversal symmetry breaking, such phonons occur at distinct frequencies.

#### S4. ANGULAR MOMENTUM OF CHIRAL PHONONS

In the main text we discussed the fact that including TRS breaking via  $\mathbf{G}$  in the equations of motion resulted in chiral phonons with well-defined angular momenta. We now analyze in more detail the angular momentum of the phonon modes shown in Fig. 1(b) in the main text. From the symmetry of CrI<sub>3</sub>, specifically the three-fold rotation axis in the out-of-plane  $z$  direction, the total angular momentum of a normal mode can only have  $z$  components. For mode  $n$ , the angular momentum is  $l_z^{(n)} = 2\hbar\text{Im}[\sum_{\tau} m_{\tau}\eta_n(\tau x)^*\eta_n(\tau y)]$ , where  $\eta_n(i\alpha)$  is the eigendisplacement component for nucleus  $i$  along direction  $\alpha$  for the  $n$ th mode. Consider, for example, the green  $E_g$  mode in Fig. 1(b) of the main text with unperturbed frequency  $\hbar\tilde{\omega} = 13.5$  meV. The angular momentum of this mode is due to the in-plane motion of iodine atoms. Choosing the two degenerate modes  $\tilde{\eta}_x$  and  $\tilde{\eta}_y$  to involve real displacements of I atoms moving in the  $x$  and  $y$  directions respectively, neither of these modes has a non-zero angular momentum by itself. However, the complex circularly polarized combination is  $\eta'_{\pm} = (\tilde{\eta}_x \pm i\tilde{\eta}_y)/\sqrt{2}$ , which corresponds to the circular displacement patterns shown in Fig. S1. In Fig. 1(c) of the main text, we plot the angular momentum of the modes after including the velocity-force coupling, with the color corresponding to the mode on the right side of Fig. 1(b). For the  $E_g$  modes near 13 meV [green and orange in Fig. 1(b)] an analysis of the displacement patterns and angular momentum of the split modes is complicated by the fact that all four modes can mix [unlike the higher-frequency split mode and the gray  $E_u$  mode above it in Fig. 1(b)]. Thus the angular momentum contributions seen in Fig. 1(c) are mixed between these modes.

A large velocity-force coupling does not necessarily result in a large phonon angular momenta after splitting, as seen for the case the lowest two  $E_g$  modes [blue curves in Fig. 1(b) of the main text]. The relatively modest angular momentum of these modes [see Fig. 1(c) of the main text] is a result of the fact that the motions of the real eigendisplacements before the inclusion of the  $\mathbf{G}$  perturbation involve *out-of-plane* motions of I atoms, not just in-plane motions like those depicted in Fig. S1. This is allowed by symmetry since individual atoms may have in-plane angular momentum components  $l_x$  and  $l_y$ , as long as these components sum to zero over all atoms. The resulting  $l_z$  is thus significantly reduced compared to the green 13.5 meV  $E_g$  mode. Note that even though the blue  $E_g$  mode is quite isolated in frequency compared to the other  $E_g$  modes, the asymmetry of  $l_z$  of the modes after splitting indicates significant mixing with these other modes.

Finally, we can see in Fig. 1(c) of the main text that higher frequency modes tend to have higher angular momentum. This is likely due to the fact that the in-plane vibrations in CrI<sub>3</sub> tend to have higher frequency, and, as pointed out above, only in-plane displacements contribute to  $l_z$ .

[S1] X. Gonze and C. Lee, *Phys. Rev. B* **55**, 10355 (1997).

[S2] S. Baroni, S. de Gironcoli, A. Dal Corso, and P. Giannozzi, *Reviews of Modern Physics* **73**, 515–562 (2001).

[S3] D. Vanderbilt, *Berry Phases in Electronic Structure Theory: Electric Polarization, Orbital Magnetization and Topological Insulators* (Cambridge University Press, 2018) Chap. 3.